Electrochimica Acta 500 (2024) 144767

Contents lists available at ScienceDirect

Electrochimica Acta

journal homepage: www.journals.elsevier.com/electrochimica-acta

Experimental determination of stray currents in parallel operated cells exemplified on alkaline water electrolysis

Deniz Dogan [a,b,*], Burkhard Hecker [a], Bernhard Schmid [a], Hans Kungl [a], Hermann Tempel [a], Rüdiger-A. Eichel [a,b]

[a] Institute of Energy Technologies - Fundamental Electrochemistry (IET-1), Forschungszentrum Jülich GmbH, Wilhelm-Johnen-Straße 1, Jülich 52428, Germany
[b] Institute of Physical Chemistry, RWTH Aachen University, Landoltweg 2, Aachen 52074, Germany

ARTICLE INFO

Keywords:
Alkaline water electrolysis
Parallel electrochemical cells
Stray current
Shunt current

ABSTRACT

Avoiding undesired electric field-driven cell-to-cell ion conduction is a common issue in electrochemical bipolar stacks affecting many processes such as alkaline water electrolysis, chlor-alkali electrolysis, and redox flow batteries. In bipolar stack systems, they are known as ionic shunt or stray currents and flow alongside a cell stack through the electrolyte manifolds bypassing the bipolar plates. A similar phenomenon occurs if multiple single cells are operated in parallel with a common electrolyte supply, even though each individual cell is galvanically isolated. If the parallel cells are operated at different voltages, an electrochemical potential gradient is formed across the electrolyte tube manifold, causing stray currents to flow from one cell to the other. It is important to determine and reduce stray currents and its implications to ensure high system efficiency and maximum system lifetime. This work presents a new approach with which stray currents between parallel operated, galvanically isolated electrochemical cells has been determined for the first time. For this purpose, an ionic 4-point measurement was implemented into an experimental setup with two electrolyzer flow cells with a common electrolyte supply using reference electrodes. This approach was used to measure the potential differences ΔE between both electrolyzers exemplarily for alkaline water electrolysis. Combined with the measured ionic resistances of the electrolyte within the polymeric tube manifold, stray currents were accurately determined. The presented results show that the ionic 4-point measurement could be successfully implemented and validated to experimentally determine stray currents between parallelly operated cells. The method presented enabled stray current measurements with high precision in the mA range. Due to the high cell currents and high ionic tube resistance, the stray current is less than 1 % in the introduced electrochemical setup. The demonstrated systematic measurement approach can be easily transferred to other electrochemical systems or processes.

1. Introduction

Ionic shunt or stray currents (SC), also referred to as parasitic, bypass, or leakage currents, typically occur in electrochemical bipolar cell stacks [1]. Such cell stacks consist of multiple electrochemical cells that are galvanically and geometrically connected in series with bipolar plates [2]. One side of a bipolar plate serves as the cathode of one cell and the other side serves as the anode of the next cell, i.e., cathode and anode of adjacent cells have approximately the same electrical potential. Due to the bipolar plates, the electrochemical potential within a cell stack builds up serially from cell to cell. The sum of the individual cell voltages is, therefore, the total voltage of a bipolar stack as shown in Fig. 1a [3]. Bipolar cell stacks are often designed with a common electrolyte supply [4]. For a common electrolyte supply system, shared flow-field channels or tube manifolds are used, which form cell-to-cell connections. Due to the bipolar structure and the electrolyte conductivity an electrochemical potential gradient is formed across these connections. Under these conditions, ions can be conducted from one cell to the adjacent cell along the ionically conductive connection thus bypassing the bipolar plates. This undesired ion conduction in electrochemical bipolar stacks is defined as ionic SC [5]. In Fig. 1a, a bipolar stack with its locally varying electrochemical potential is shown, which provides an ionic SC pathway due to a common electrolyte supply system (red line).

* Corresponding author at: Institute of Energy Technologies - Fundamental Electrochemistry (IET-1), Forschungszentrum Jülich GmbH, Wilhelm-Johnen-Straße 1, Jülich 52428, Germany.
E-mail address: d.dogan@fz-juelich.de (D. Dogan).

https://doi.org/10.1016/j.electacta.2024.144767
Received 19 January 2024; Received in revised form 22 July 2024; Accepted 24 July 2024
Available online 25 July 2024

Abbreviations and symbols

Abbreviations

AWE	alkaline water electrolysis
EPDM	ethylene propylene diene monomer
FEP	fluorinated ethylene propylene
PEEK	polyether ether keton
PEIS	potentiostatic electrochemical impedance spectroscopy
PP	polypropylen
PTFE	polytetrafluorethylen
SC	stray current
SHE	standard hydrogen electrode
WE	working electrode

Latin symbols

d	diameter
A	area
E	electrode potential
E(x)	distance-dependent electrochemical potential
I	current
i	current density
l	length
R	ionic resistance
T	temperature
U	cell voltage

Greek symbols

Δ	difference
σ	specific conductivity

Subscripts

a	anode
aa	between anode and anode
c	cathode
cc	between cathode and cathode
cross	cross-sectional
d	dynamic
ext	extension
i	inner
s	steady state
sc	stray current
t	tube

Superscripts

o	standard

A similar phenomenon can occur in a system where electrochemical cells are operated in parallel, i.e., each cell has its own potentiostat for power supply and electrochemical analysis. In such a system, all cells are galvanically isolated. However, in the case of a common electrolyte supply, the individual cells are ionically connected to each other. This ionically conductive cell-to-cell connection again serves as a pathway for undesired ion conduction from one cell to another (Fig. 1b). Unlike the bipolar stack, under ideal operating conditions the electrochemical potentials of parallel single cells do not build up serially due to the absence of a galvanic connection. Rather, the electrochemical fields are freely aligned with each other. In this system, undesired ion conduction, therefore, only occurs if different cell voltages are applied, or the cells

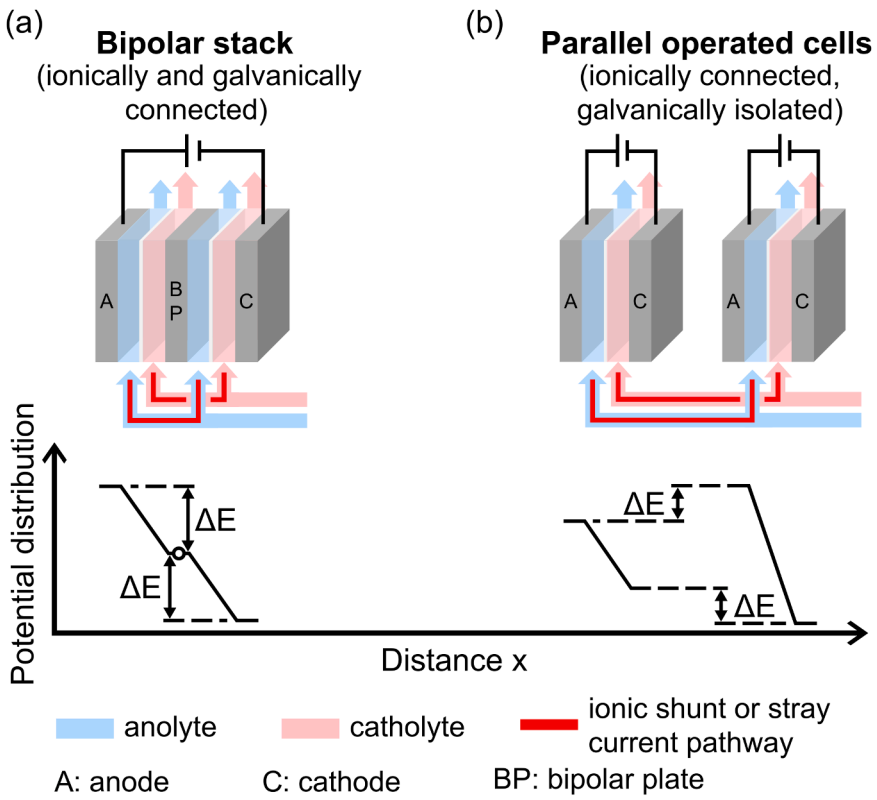

Fig. 1. Two different electrochemical systems that provide ionically conductive connections and potential differences between adjacent cells enabling shunt or stray current formation: Electrochemical stack with a bipolar plate that galvanically connects the cells and thereby builds up serially the total electrochemical stack potential (a). Parallel operated cells that are galvanically isolated with electric fields that are freely aligned with each other (b).

are not identical. Different cell voltages can be applied to efficiently distribute power among parallel operated systems in order to increase system efficiency and reduce the cost of production [6].

As discussed, the two systems described differ from each other. In the case of bipolar stacks, the term ionic shunt current is most commonly used to describe this phenomenon. Occasionally used, but less common in the context of bipolar stacks, is the term stray currents. In bipolar stacks, the ionic SC bypasses the bipolar plates, however the origin and destination (terminal cathode and terminal anode) of the ionic SC is identical to that of the ionic cell current. In a system with galvanically isolated cells operated in parallel, a part of the ionic cell current of one cell rather strays into the parallel operated cell. The phenomenon in such a system as considered in this publication is, therefore, better described by the term stray current and will be used in the following. Fig. 1 shows both systems, a bipolar stack and single cells operated in parallel, with an ionic SC pathway (red line) and a schematic illustration of the electrochemical fields of the individual cells.

It should be noted that galvanically isolated single cells in parallel operation (Fig. 1b) are no industrial arrangement. In industry, single cells are electrically connected to bipolar stacks (Fig. 1a) for economic reasons [7]. However, there are commercial arrangements in which several bipolar stacks are operated in parallel [8]. This industrial arrangement represents a mixture of both systems shown in Fig. 1. In this study, the arrangement of parallel, galvanically isolated single cells is investigated. It is used as a simplified, bespoke arrangement. The findings derived from here can be transferred to the industrial application mentioned above.

The magnitude of SC in an electrochemical system with common electrolyte supply depends on the total number of cells in the system, magnitude of cell voltages, electrolyte conductivity and geometry of the tube manifold. [9] Depending on the type of electrochemical system, SC can cause:

- decrease in Faraday efficiency and overall energy efficiency [10],
- accelerated aging at electrode regions near to the electrolyte inlets and outlets particularly of the terminal electrodes induced by locally above-average current densities [11,12],
- non-uniform voltage and current distribution in stacks, leading to different cell performances depending on the cell position within the stack [13],
- interference with instrumentation, undesirable gas formation or corrosion of metallic components [5,14,15], and
- explosive or flashover voltage hazard [1,16].

Avoiding the implications of SC plays an important role in ensuring maximum system lifetime and system efficiency. Therefore, the determination of SC for the design of electrochemical multi-cell systems is important. In the literature, two approaches can be found to quantify SC, i.e. a theoretical, model-based method and experimental approaches. The former was first pursued in the 1940s, where an equivalent circuit model was proposed to describe an electrochemical system [17]. Using equivalent circuit models, SC can be determined based on Kirchoff's law. In 1976, an equivalent circuit model was developed for NASA to estimate SC in redox flow battery systems [4]. In the following decades, this approach was adapted [18] and published for Fe/Cr redox flow battery [19,20] and fuel cell systems [21–24]. Further studies show equivalent circuit model based SC determination in Vanadium redox flow batteries [5,25,26]. For the quantification of SC, most studies are based on the theoretical approach. Few publications demonstrate the experimental determination of SC. For experimental quantification, for instance magnetic field detectors were used to measure the magnetic field generated by SC [27]. Only a few research groups determined the potential difference or directly SC through the electrolyte in the tube manifold [28,29]. One research group investigated experimentally and computationally the effect of SC on the primary and secondary current distribution at the electrodes in an undivided bipolar stack [30,31]. The cited literature on the theoretical or experimental determination of SC focuses almost exclusively on bipolar stack systems (Fig. 1a). For economic reasons, electrochemical cells are commonly operated as bipolar stacks in industry [7]. In this case, multiple stacks can be connected in parallel [8]. However, ionic SC formation between parallel operated systems has hardly been studied. One publication focused on SC between parallel bipolar electrolysis stacks [6]. There are only a few publications investigating SC in the field of alkaline water electrolysis (AWE) [6,32].

The aim of this work was the development of an ionic 4-point measurement to experimentally investigate SC formation between parallel operated electrochemical systems. For this purpose, a simplified, bespoke setup with two galvanically isolated, parallel operated cells was used. The introduced ionic 4-point measurement approach is based on the simultaneous use of four reference electrodes. The advantage over measurements with magnetic field detectors [27] or current sensors [29] for example, is the high measurement accuracy at low investment costs. The measurement technique was implemented into the bespoke setup with two parallel electrolysis flow cells and exemplarily validated for alkaline water electrolysis (AWE). The findings of this simplified setup will help to better understand SC formation occurring in industrial relevant systems such as parallel operated bipolar stacks. The presented measurement technique is a systematic and transferable approach that can be easily applied to other electrochemical systems or processes.

2. Methods

An ionic 4-point measurement was set up to determine the potential difference ΔE of adjacent electrodes between parallel, galvanically isolated electrochemical cells. For this purpose, modified electrolyte flow fields (cf. supplementary information) with a narrow groove were implemented into the flow cells. Reference electrodes were placed in external electrolyte vessels connected to the cells via Haber-Luggin capillaries made of PEEK with an inner diameter of 0.5 mm. These capillaries were passed through the grooves of the flow fields directly in front of the electrodes. Each cell was equipped with two reference electrodes. The application of this ionic 4-point measurement enables the determination of the potential difference ΔE of adjacent anodes and adjacent cathodes of parallel electrochemical flow cells. Fig. 2 shows the schematic illustration of the 4-point measurement implementation in an experimental setup with two electrolyzer flow cells that was used for this study.

Operating parallel, galvanically isolated cells with individual current or voltage source and a common electrolyte supply requires appropriate operating modes of the potentiostats. Important for the voltage or current sources used in such a setup is that the electrical devices can be operated in grounded and floating mode. Therefore, either multiple potentiostats or individual channels of a multipotentiostat that provides this function can be used. The default setting for single-cell experiments with a cell that is not self-grounded is the grounded mode. If additional cells are operated electrically in parallel with a common electrolyte supply, it is particularly important that each additional flow cell is operated galvanically isolated from the first. For such a system, the operating mode of the potentiostat of each additional cell must be set to floating mode (Fig. 3a). Multiple potentiostats operated in grounded mode within the same electric circuit are connected via ground. This connection can have a direct effect on the alignment of the electric fields of the individual cells, which in turn could affect the potential difference ΔE between galvanically isolated parallel cells with a common electrolyte supply. A potentiostat is typically grounded via the connection of the working electrode (WE). When multiple potentiostats are parallel operated in grounded mode, the alignment of the electric fields to each other is essentially determined by which electrodes are set as WE (Fig. 3b and 3c). Three cases for two parallel, galvanically isolated flow cells with different potentiostat settings and their effect on the alignment of the electric fields to each other are shown in Fig. 3. All experiments in this study with two cells in parallel operation were performed with one cell grounded and the second floating as shown in Fig. 3a.

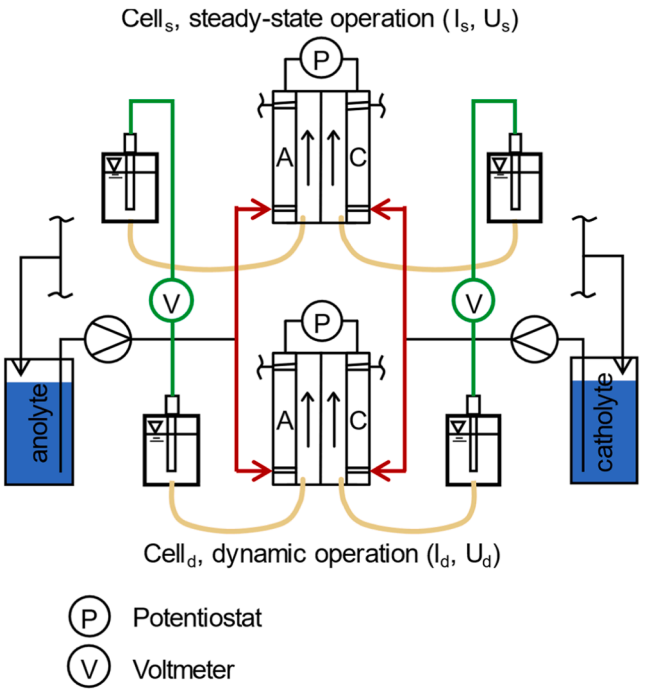

Fig. 2. Schematic illustration of the ionic 4-point measurement for SC determination performed between two electrolyzer flow cells. Both cells were connected to individual channels of a multichannel potentiostat (P) and supplied with common electrolyte feeds. Tube manifolds of the supply system present ionically conductive connections providing SC pathways (red line). Potential differences of adjacent electrodes were measured with a voltmeter (V, green line) and reference electrodes.

3. Experimental

All AWE experiments were conducted with Micro Flow Cells® from ElectroCell A/S (Tarm, Denmark). The anode and cathode compartments were built identically, each comprising a Ni electrode, PTFE flow field and EPDM gaskets. The separator was a Zirfon Perl UTP 500 diaphragm from Agfa-Gevaert N.V. (Mortsel, Belgium). The electrode surface area and electrolyte chamber thickness were 10 cm^2 and 2 mm, respectively. For all experiments, 6 M KOH (p.a. quality, Merck) solution was prepared and used as anolyte and catholyte. The electrolytes were freshly prepared before each experiment with deionized water from a PURELAB® flex system. 250 ml each of anolyte and catholyte were circulated separately using a peristaltic pump at a flow rate of 100 ml/min (equivalent to 10 ml/min/cm^2) per cell. The overall supply system was built entirely of FEP or PP polymer parts. The inner diameter of all tubes was 4 mm. Oxygen and hydrogen gas formed was diluted and displaced from the feed reservoirs with an argon flow of 50 mL/min. A single-cell setup was used to characterize the electrolyzer without any disturbances occurring during parallel operation. All other AWE experiments were performed with the two-cell setup with common electrolyte supply (Fig. 2).

For the two-cell experiments, the electrolyzers were operated with two channels of a VSP-300 potentiostat from Bio-Logic SAS (Seyssinet-Pariset, France). The operating mode of the potentiostat was set to grounded mode for one cell and floating mode for the second cell during the experiments (Fig. 3a). The configuration was verified with a breadboard and electrical resistors. During the two-cell experiments, one cell was continuously operated under steady state conditions (cell$_s$), while the operating parameters of the second cell were varied (cell$_d$). The cells were operated in either potentiostatic or galvanostatic mode, depending on the experiment. Before measuring the potential difference between adjacent cells, both cells were conditioned at 100 mA/cm^2 for one hour after preparation of the experimental setup. After system conditioning, cell$_d$ was operated at different current densities. The

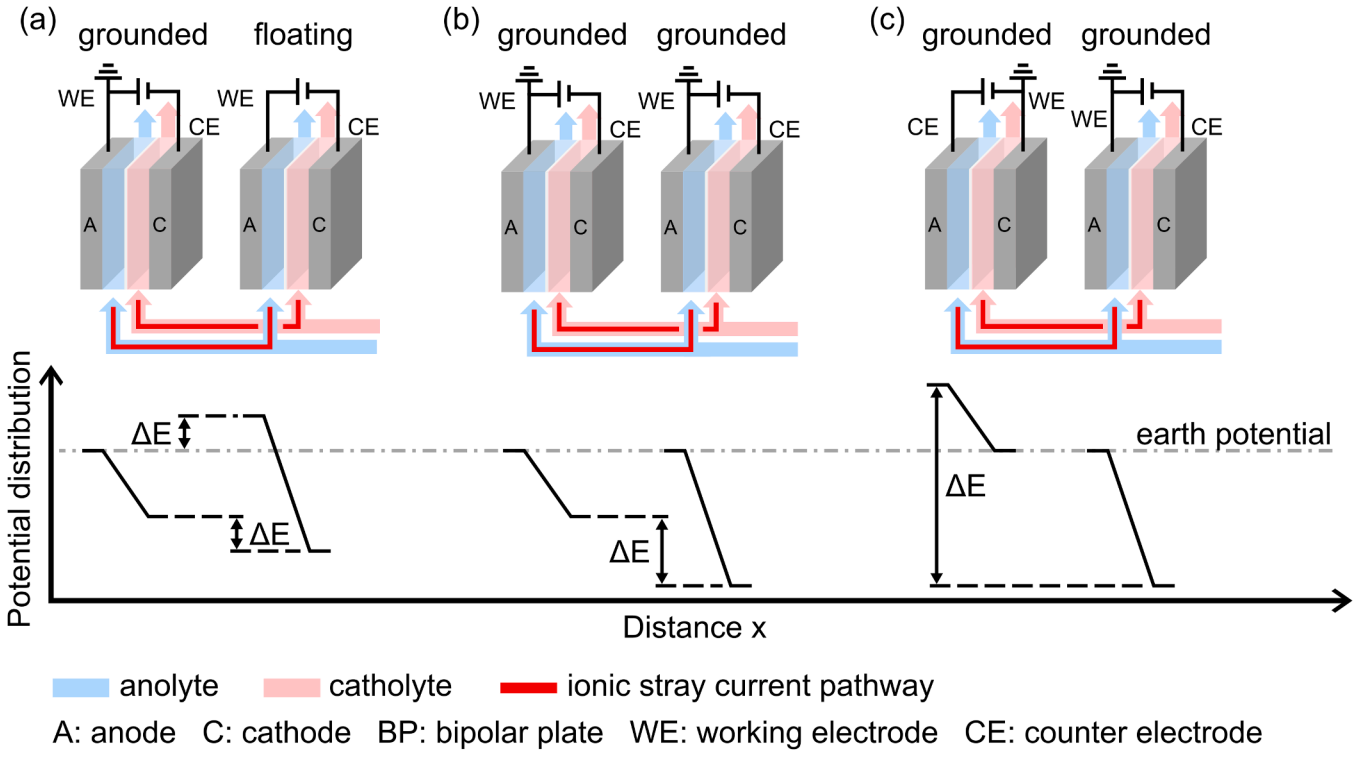

Fig. 3. Effect of potentiostat operating modes for two parallel, galvanically isolated but ionically connected cells on the alignment of the individual electric fields to each other. Three different cases: one cell grounded to earth and one cell floating (a), both cells grounded to earth with anodes connected via grounding of working electrodes (b) as well as both cells grounded to earth with one anode and one cathode connected via grounding of working electrodes (c).

corresponding signals were recorded after 10 min when steady state conditions were reached. The mean value and standard deviation calculated in the experimental data are based on a series of 3 measurements per measuring point. Hg/HgO reference electrodes type RE-61AP from ALS Co., Ltd (Tokyo, Japan) were used to measure electrode potentials or potential differences and were filled and conditioned with 6 M KOH solution. All measured potentials were converted to the potential against the standard hydrogen electrode (SHE). The electrode potentials of the Hg/HgO reference electrodes (78.5 mV vs. SHE) were determined and regularly checked experimentally using reference electrodes with well-defined potentials. Potential differences between adjacent electrodes were measured using a 175 True RMS multimeter from Fluke Corporation (Everett, USA). All measured electrode potentials for cathode or anode vs. Hg/HgO reference electrodes were IR drop corrected. The required ohmic resistances between Ni electrode and reference electrode were determined by potentiostatic electrochemical impedance spectroscopy (PEIS) in a three-electrode setup. All resistance values between Ni electrodes of adjacent cells required for SC calculations were measured by PEIS in a two-electrode setup. All PEIS measurements were performed in the range of 0.1 to 1E+05 Hz at E or U = 0 V and an electrolyte flow of 10 ml/min.

4. Results and discussion

In order to characterize an individually operated single AWE cell, I-U and electrode polarization curves were recorded and are depicted in Fig. 4. The cell voltage U (a) and electrode potentials E_a/E_c (b) are depicted as a function of the current density i. Dashed lines indicate the thermoneutral cell voltage of the overall reaction $U^o = 1.23$ V, and the thermoneutral electrode potential of the oxygen evolution reaction $E_a^o = 0.336$ V and hydrogen evolution reaction $E_c^o = -0.894$ V vs. SHE. U shows a characteristic course with a non-linear and linear region at $i < 50$ mA/cm^2 and $i \geq 50$ mA/cm^2, respectively. At 500 mA/cm^2 U reaches a value of 3 V. The actual values of the onset potentials of E_a and E_c exceed the respective thermoneutral potentials. E_a and E_c reach electrode potentials of 0.86 V and −1.79 V vs. SHE at 500 mA/cm^2, respectively.

The cell voltage (Fig. 4a) of the electrolyzer is affected by different mechanisms, i.e. ohmic losses, activation losses, and mass transport losses [33]. Ohmic losses occur in the electrolyte due to its ionic resistance and cause the characteristic linear trend of the cell voltage at higher current densities. The electrode polarization curves E_a and E_c (Fig. 4b) do not include ohmic losses, but do include activation and mass transport losses, which are also referred to as overpotentials. Activation overpotentials increase the onset voltage of the electrolyzer and correspond to the activation barrier of the electrochemical half reaction. They are affected by the type of reaction and material properties. Their physicochemical relation can be described by the Butler-Volmer equation. Activation overpotentials are predominant in the low current density range and lead to the non-linear behavior of U, E_a, and E_c in this region. Mass transport overpotentials arise increasingly when the diffusive and convective mass transport of the reactants to the electrodes and of the products into the electrolyte solution is slower than the reaction rate [34,35].

Parallel operated electrolysis cells can measurably interfere with each other if they are operated with a common electrolyte supply. These interferences are shown in Fig. 5, where the effect of an increasing cell voltage difference $\Delta U = U_d - U_s$ on the cell current I_s of $cell_s$ was measured. $Cell_s$ was operated under steady state conditions at a constant low voltage with $U_s = 1.5$ V during the entire experiment. I_s was recorded as U_d was incrementally increased. Initially both cells were operated at constant voltages of $U_d = U_s = 1.5$ V ($\Delta U = 0$) for 1 h (Fig. 5). After the conditioning period, U_d is increased from 1.5 V in 0.1 V increments every 15 min until U_d reaches 2.5 V after 3.5 h. After one hour with the increase in ΔU, a sudden drop in I_s can be observed in Fig. 5. This effect gradually diminishes with each further increase in the cell

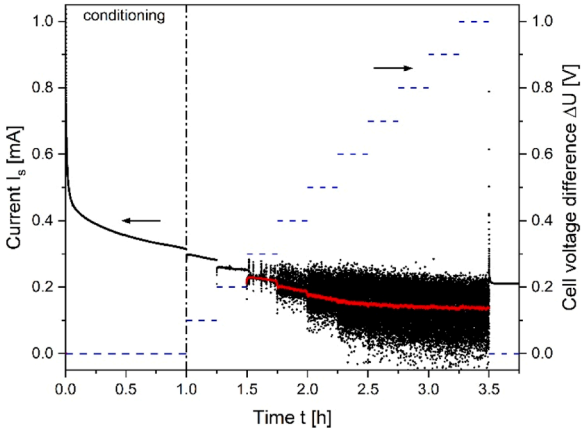

Fig. 5. Investigation of the effect of deliberately increased cell voltage difference $\Delta U = U_d - U_s$ on cell current I_s. I_s (left axis) at a constant cell voltage $U_s = 1.5$ V at all times with moving average (red line) and ΔU (right axis) are depicted as a function of time t. $Cell_d$ voltage U_d was increased by $\Delta U_d = \Delta U = 0.1$ V every 15 min starting from $U_d = U_s = 1.5$ V up to $U_d = 2.5$ V. After 3.5 h ΔU was reset to 0 V.

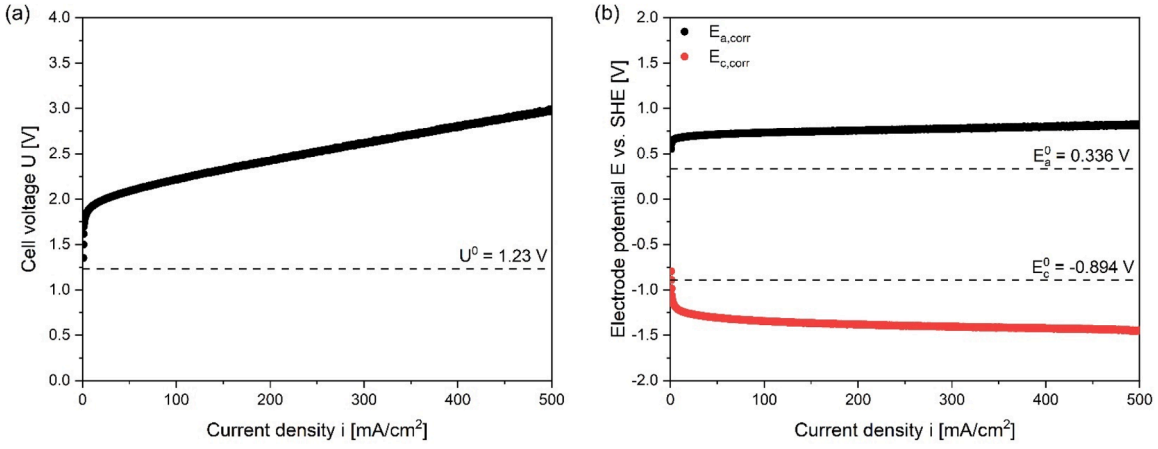

Fig. 4. Cell voltage U (a) as well as anode and cathode electrode potential E vs. SHE (b) as a function of current density i measured in a single cell for AWE at 25 °C. Data were recorded using a linear scan (scan rate = 1 mA/s, step size = 2 mA). Dashed lines indicate the thermoneutral cell voltage of the overall reaction $U^0 = 1.23$ V as well as thermoneutral electrode potentials of the oxygen evolution reaction $E_a^0 = 0.336$ V and the hydrogen evolution reaction $E_c^0 = -0.894$ V for AWE.

voltage difference. Furthermore, starting from $\Delta U = 0.3$ V the I_s signal becomes noisy. The noise intensity of I_s amplifies with an increase in ΔU. At high values of ΔU, I_s approaches 0.13 mA as shown by the moving average (red line, Fig. 5). After 3.5 h, the cell voltage difference is reset to $\Delta U = 0$ V and maintained for 15 min. Due to the sudden reset of ΔU, the current I_s in $cell_s$ rises abruptly and reaches 0.21 mA after 3.75 h. Furthermore, the noise stops immediately and the I_s signal continues undisturbed. The voltage dependent current of the dynamic cell I_d can be obtained approximately from Fig. 4a.

In conventional single-cell operation, the electric field is formed within the cell between the anode and cathode. In the setup presented here, the tube manifolds provide ionically conductive connections between the two cells operated in parallel. This arrangement leads to more complex electric field formations in the setup presented. The electric fields of the individual cells can expand through the tube manifolds and superpose each other. Furthermore, secondary electric fields can be formed between adjacent electrodes of the two parallel cells. The weak electric field of a cell at low cell currents is interfered by these complex electric field formations. As observed, even small differences in cell voltage can therefore change the cell current and lead to noise in the current signal (Fig. 5). As the cell current increases, the influence of the electric field of the adjacent cell decreases. Measurement data at higher start cell voltages are shown in the supplementary information (Fig. S2 and S3). As both interference effects disappear immediately when the cell voltage difference is reset ($\Delta U = 0$), it can be ruled out that the interferences are caused by other phenomena such as adsorption or foreign gas bubbles.

Next, the potential differences between the electrodes of the parallel AWE cells were measured. In Fig. 6, the voltmeter measurements between the reference electrodes located in the vicinity of the two anodes ΔE_{aa} and between the reference electrodes located in the vicinity of the two cathodes ΔE_{cc} (see Fig. 2) are depicted as a function of the applied current density of the dynamic cell i_d. During the entire experiment, the steady state cell was operated at $i_s = 100$ mA/cm^2. ΔE_{aa} and $-\Delta E_{cc}$ show a linear course for $i_d \geq 50$ mA/cm^2 and a nonlinear course for $i_d < 50$ mA/cm^2. In the linear region, the correlation $\Delta E_{aa} = -\Delta E_{cc}$ can be observed. For a current density value of $i_d = i_s = 100$ mA/cm^2, the potential difference ΔE_{aa} and $-\Delta E_{cc}$ are both approximately zero. As i_d increases, ΔE_{aa} and $-\Delta E_{cc}$ increase linearly and reach a potential difference of about 280 mV at $i_d = 500$ mA/cm^2. In the nonlinear region, both quantities show a divergent course. Deviating from the linear course, ΔE_{aa} decreases more rapidly and shows a steep drop as i_d approaches 0 mA. Opposed to this, the curve of $-\Delta E_{cc}$ initially becomes flatter in the low current range as i_d decreases. For very small values of i_d, $-\Delta E_{cc}$ increases slightly.

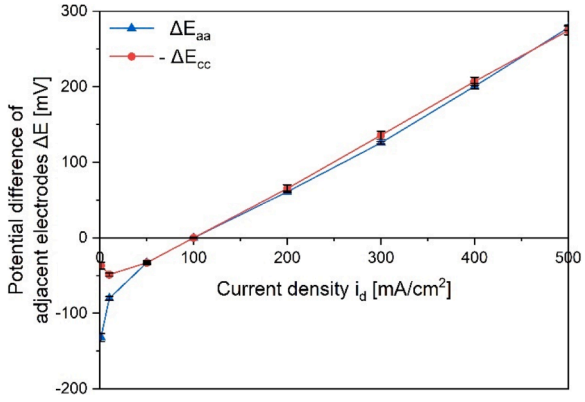

Fig. 6. Potential difference of adjacent anodes ΔE_{aa} (blue line) and adjacent cathodes $-\Delta E_{cc}$ (red line) as a function of current density i_d. Current density i_d of $cell_d$ was stepwise increased from 1 up to 500 mA/cm^2. $Cell_s$ was constantly operated at $i_s = 100$ mA/cm^2. ΔE was measured at 25 °C.

As can be observed, ΔE_{aa} and $-\Delta E_{cc}$ are asymmetric at low current densities of the dynamic cell ($i_d < 50$ mA/cm^2). This asymmetry in the measurement of potential differences is an indicator of an increased gas crossover. In water electrolysis, gas crossover describes the transport of hydrogen and oxygen in the cell through the separator to the opposite electrolyte compartment and is caused by different mechanisms. In the system of this study, the predominant mechanism for this effect is the differential pressure of the gases in the respective electrolytes. [36] Due to the mixing in the electrolyte reservoir and common electrolyte supply, the hydrogen differential pressure in the catholyte and therefore the hydrogen gas crossover through the separator into the anolyte is equal in both cells. The same applies to the oxygen crossover. Thus, at low current densities ($i_d < 50$ mA/cm^2), the gas crossover rate in the dynamic cell is relatively high. Since the hydrogen is partially oxidized at the anode and the oxygen is partially reduced at the cathode, this effect results in an additional charge transfer from the steady state cell to the dynamic cell. At very low current densities of the dynamic cell, this charge transfer affects the measured potential differences ΔE_{aa} and $-\Delta E_{cc}$ and causes the asymmetric curve. Detailed explanations of this hypothesis with the corresponding calculations are provided in the supplementary information.

The distance-dependent electrochemical potential E(x) within the cells is schematically depicted in Fig. 7. The potential profile is divided into five regions (I - IV). The overpotentials characteristic for these regions are shown for the steady state cell (solid line) and dynamic cell (dotted line). The depicted curves are based on the data for the operating conditions $i_s = 100$ mA/cm^2 and $i_d = 10$ mA/cm^2 (a) as well as $i_s = 100$ mA/cm^2 and $i_d = 500$ mA/cm^2 (b). The anode overpotential drops in the vicinity of the anode surface (I). The electrode overpotential is composed of the activation and concentration overpotential. Both overpotentials are merged and shown as one curve in Fig. 7. However, under the selected operating conditions, the activation overpotential predominates, as the process is not mass transport limited (Fig. 4a). The overpotentials over the anolyte (II) and the separator (III) are characterized by ohmic drops. The same overpotentials of the anode side occur on the cathode side (IV, V). Due to the symmetrical cell structure, the potential profile is almost rotation symmetrical. Only the electrode overpotentials deviate from each other (Fig. 4b). The dimensions of distance x of the individual regions I - V in Fig. 7 are not true to scale for improved visualization.

With increasing current density, the individual overpotentials I - V increase. Therefore, the potential profiles of the steady state and the dynamic cell differ in Fig. 7. The potential difference between the potential in the steady state cell $E_s(x)$ and the potential in the dynamic cell $E_d(x)$ increases towards the respective electrodes. It can be seen that the contribution of the ohmic overpotentials to this effect is greater than that of the electrode overpotentials. It should be noted that this assumption is only valid for the operating conditions shown (no mass transport limitation). The measurement of the potential differences ΔE_{aa} and ΔE_{cc} was conducted between two reference electrodes in the vicinity of the respective electrodes. The measured values ΔE_{aa} (red line) and ΔE_{cc} (blue line) are highlighted in color in Fig. 7. Since measurements were not conducted between reference electrode and cathode or anode, but between both reference electrodes, changes of the difference of the electrode overpotentials are not taken into account in the measurement. However, the effect of the changes caused by the electrode overpotentials on the measurement is negligible as discussed.

Fig. 8 shows the results of the investigation of the temperature effect on the measured potential differences. Depicted are ΔE_{aa} (a) and $-\Delta E_{cc}$ (b) as a function of i_d at 25, 40 and 60 °C. The experimental results indicate that an increase in temperature leads to a decrease in $|\Delta E|$, i.e. for $i_d > i_s$, ΔE_{aa} and $-\Delta E_{cc}$ decrease as T increases. For $i_d < i_s$, ΔE_{aa} and $-\Delta E_{cc}$ increase to less negative values as T increases. The temperature effect can be observed to the same extent for both ΔE_{aa} and $-\Delta E_{cc}$. At $i_d = 500$ mA/cm^2, ΔE_{aa} and $-\Delta E_{cc}$ reach a potential difference of about 280, 220 and 170 mV at 25, 40 and 60 °C, respectively.

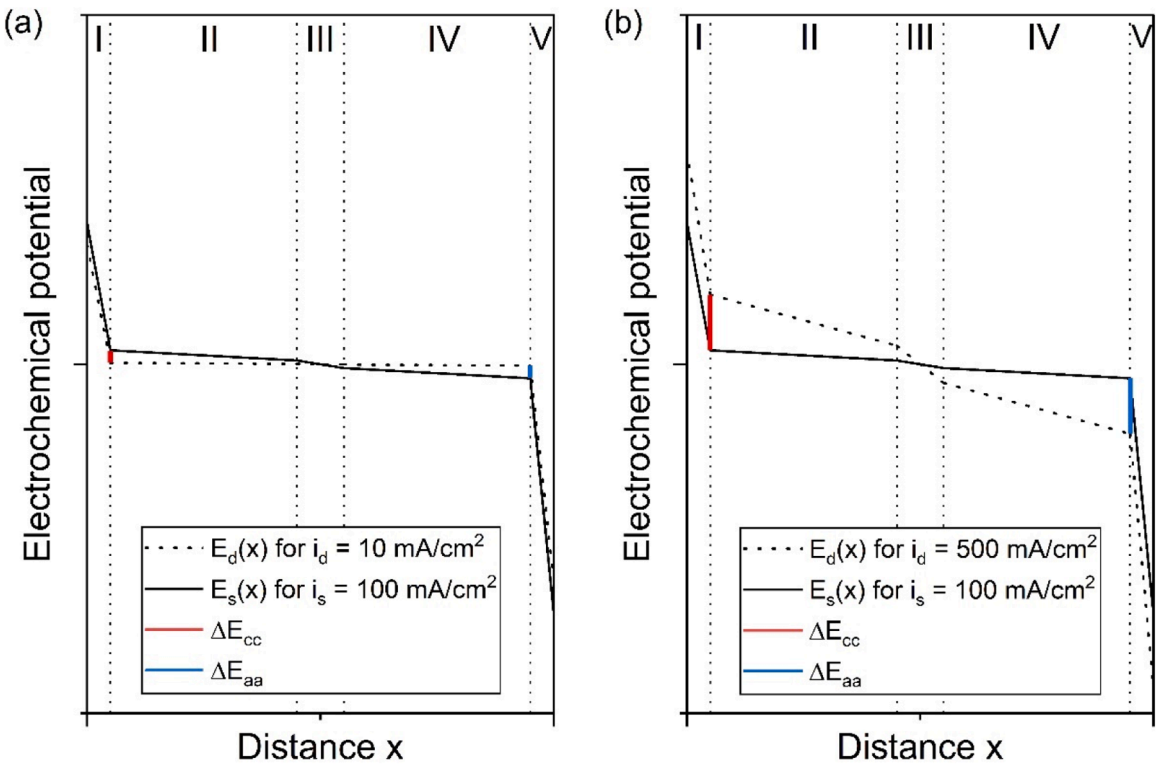

Fig. 7. Schematic representation of the distance-dependent electrochemical potential E(x) within the symmetric AWE cells for two different current density values i_d of $cell_d$. Operating conditions in the figure are i_s = 100 mA/cm^2 and i_d = 10 mA/cm^2 (a) as well as i_s = 100 mA/cm^2 and i_d = 500 mA/cm^2 (b). The potential distributions are depicted as a function of the distance x in the electrochemical field and shown for the steady state cell $E_s(x)$ (solid line) and dynamic cell $E_d(x)$ (dotted line). The potential distribution is composed of the electrode overpotential of the anode (I), ohmic overpotential in the anolyte (II), ohmic overpotential in the separator (III), ohmic overpotential in the catholyte (IV) and electrode overpotential of the cathode (V). Values for the individual overpotentials were taken from experimental data and literature. The dimensions of the individual regions I - V are not true to scale for improved visualization.

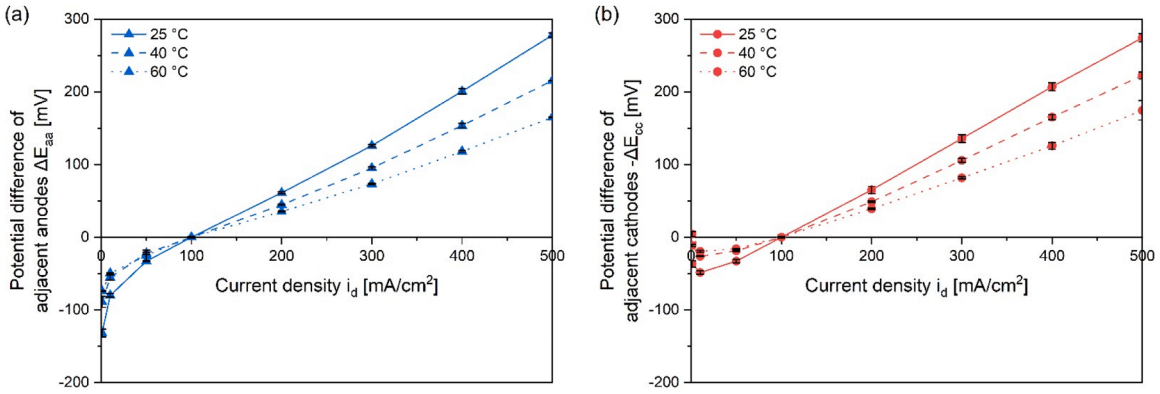

Fig. 8. Potential difference of adjacent anodes ΔE_{aa} (a) and adjacent cathodes -ΔE_{cc} (b) as a function of current density i_d. Current density i_d of $cell_d$ was stepwise increased from 1 up to 500 mA/cm^2. $Cell_s$ was constantly operated at i_s = 100 mA/cm^2. ΔE was measured at 25 °C (solid line), 40 °C (dashed line) and 60 °C (dotted line).

With increasing temperature, the ionic mobility increases resulting in lower ionic resistance of the electrolyte, i.e. the ionic cell resistance gradient dE/di decreases. As a result, the measured potential differences ΔE_{aa} and -ΔE_{cc} between both cells decrease with increasing temperature. The decrease of ΔE_{aa} and -ΔE_{cc} at constant current density is approximately proportional to the temperature increase. Apart from the ionic resistance of the electrolyte within the cells, the activation overpotentials are also affected by the temperature change. [37–39] However, these effects are negligible.

In order to calculate the SC I_{sc} between both cells based on the ΔE values, the ionic resistance of the electrolyte within the tube manifold between adjacent electrodes R_t is required. For this purpose, tube extensions with a defined length $l_{t,ext}$ of 10, 20 and 30 cm were installed between the electrolyte inlets and outlets of the cells (cf. supplementary information, Fig. S4). The experimental data (squares) for one of the four identical tube manifolds is depicted in Fig. 9a. The results show a linear dependence between R_t and $l_{t,ext}$. Literature data on KOH conductivity was used to calculate the theoretical value of the length-dependent resistance $dR_t/dl_{t,ext}$ for the given dimensions of the tube extension. The theoretical value of $dR_t/dl_{t,ext}$ is equal to 12.7 Ω/cm at 25 °C. $dR_t/dl_{t,ext}$ was used for the implementation of a linear fit on the experimental data (solid line). The experimental data are in very good

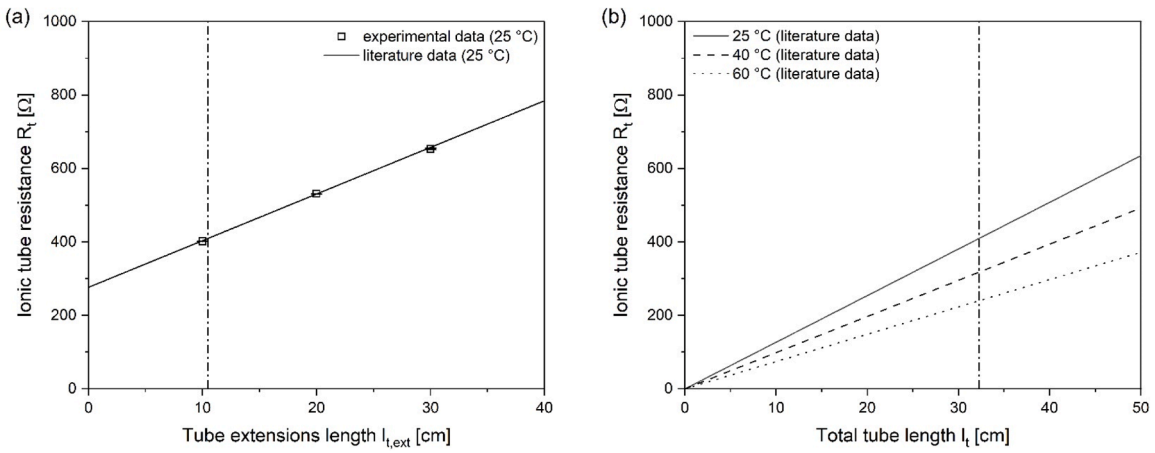

Fig. 9. The ionic tube resistance R_t as a function of tube extension length $l_{t,ext}$ (a) and total tube length l_t (b) at different process temperatures T. Inner diameter d_i of the interconnecting tube was 4 mm. The ionic tube resistance R_t was experimentally determined for $l_{t,ext}$ values of 10, 20 and 30 cm (a, squares) at 25 °C. Theoretical values of R_t at 25, 40 and 60 °C (b) were calculated based on specific conductivity values $\rho_{6M\ KOH}$ of 6 M KOH taken from literature [40]. During the experiment, R_t = 410 Ω was measured with the experimental setup (Fig. 2) of this study (dashed-dotted line).

agreement with the literature data [40]. As $l_{t,ext}$ represents only a part of the total resistance, the line does not pass through the origin. The intersection with the ordinate corresponds to the resistance of the tube connectors and is equal to 277 Ω. The vertical dash-dotted line shows the experimental condition for the ΔE measurements. Given the very good agreement with the literature, R_t at elevated temperatures was subsequently calculated using the literature data [40]. Fig. 9b shows R_t as a function of total tube length l_t for 25, 40 and 60 °C. The length dependence of R_t at elevated temperatures is 9.9 and 7.4 Ω/cm at 40 and 60 °C, respectively. R_t measured during the ΔE measurements corresponds to a length of l_t = 32.25 cm (dashed-dotted line).

SC were determined by dividing ΔE values (Fig. 8) by R_t data (Fig. 9). The total SC I_{sc} is calculated by summing the respective SC values for the common inlets and outlets of the anode and cathode sides (cf. supplementary information S5). The results of the SC calculations are depicted in Fig. 10, showing I_{sc} as a function of i_d at 25, 40 and 60 °C. When both cells are operated at the same current density ($i_d = i_s = 100$ mA/cm^2), no SC flows between the cells (I_{sc} = 0). With increasing i_d, I_{sc} increases linearly and reaches a value of I_{sc} = 2.75 mA at i_d = 500 mA/cm^2. For values i_d < 100 mA/cm^2 I_{sc} decreases linearly to negative values. A change in the process temperature has no major effect on I_{sc}.

The course of I_{sc} is determined by ΔE and accordingly by the course of the polarization curves. The linear course at high current densities is a result of the linearity of E_a and E_c in the ohmic loss range (Fig. 4). In the low current range, the nonlinearities of ΔE_{aa} and ΔE_{cc} compensate each other due to their opposite trends and lead to a linear progression of I_{sc} when calculating the total SC. Due to the increasing conductivity, |ΔE| (Fig. 8) and R_t (Fig. 9) decrease with increasing process temperature. However, the change in |ΔE| and R_t per temperature unit is the same for both variables. Thus, both effects neutralize each other, and the temperature has no relevant influence on I_{sc}.

Since I_{sc} is inversely proportional to R_t, I_{sc} is affected both by the conductivity of the electrolyte and by the tube geometry. Fig. 11 shows the influence of the tube length l_t and the inner tube diameter d_i on I_{sc}. The presented data of I_{sc} are valid for i_d = 100 mA/cm^2 and i_s = 500 mA/cm^2. The results indicate that the limit of $I_{sc}(l_t, d_i)$ is infinity as l_t approaches 0 or d_i approaches infinity. The limit of $I_{sc}(l_t, d_i)$ is 0 as l_t approaches infinity or d_i approaches 0. The experimental conditions of the ΔE measurements correspond to l_t = 32.25 cm, d_i = 4 mm and I_{sc} = 2.75 mA and are marked in Fig. 11 (red triangle).

Decreasing the tube length to l_t = 0 or increasing the inner diameter to d_i = ∞ will result in infinitely large SC, since these conditions correspond to a short circuit of the cells. Full isolation (I_{sc} = 0) is achieved by infinitely long tubing (l_t = ∞) or an inner diameter of d_i = 0. The results show that both an increase in l_t and a decrease in d_i are

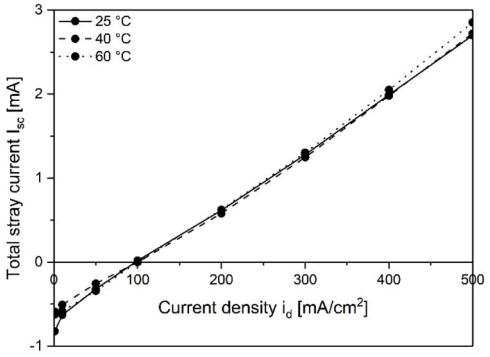

Fig. 10. Total stray current I_{sc} as a function of current density i_d between two AWE cells. Current density i_d of $cell_d$ was stepwise increased from 1 up to 500 mA/cm^2. $Cell_s$ was constantly operated at i_s = 100 mA/cm^2. I_{sc} was calculated based on ΔE measurements and R_t data. I_{sc} is depicted for 25 °C (solid line), 40 °C (dashed line) and 60 °C (dotted line).

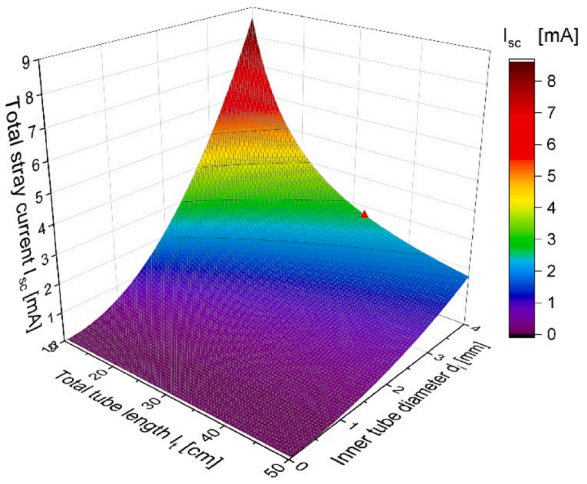

Fig. 11. Calculated total stray current I_{sc} as a function of total tube length l_t and inner tube diameter d_i between two AWE cells for i_d = 100 mA/cm^2 and i_s = 500 mA/cm^2. Tube length l_t and inner tube diameter d_i was changed from 10 up to 500 cm and 0 up to 5 mm, respectively. Experimental conditions are marked at l_t = 32.25 cm and d_i = 4 mm (red triangle).

appropriate measures to reduce I_{sc} present in a system. In practice, in some cases large values for l_t are selected to reduce I_{sc}, which may require the connecting tubes to be rolled up. When decreasing d_i, the required increase in pumping power must be taken into account.

SC are determined using Ohm's law. This equation can be rearranged (1) to determine the tube geometry (total tube length l_t and inner diameter d_i) required to reduce the total SC I_{sc} to a defined limit, where $\sigma_{electrolyte}$ is the specific conductivity of the electrolyte and $A_{t,cross}$ the cross-sectional area of the tube.

$$l_t = 4 \cdot \sigma_{electrolyte} \cdot A_{t,cross} \frac{\Delta E}{I_{sc}} \quad (1)$$

If I_{sc} in the system presented is to be reduced to 1 mA during operation with $i_s = 100$ mA/cm^2 and $i_d = 500$ mA/cm^2, a minimum tube length of 87.0 cm is required when using 6 M KOH and a tube inner diameter of 4 mm. The measurement approach introduced can be applied to other electrochemical systems to experimentally determine ΔE. Eq. (1) can then be used to determine the tube geometry needed to avoid negative SC implications.

5. Conclusions

In this study, the ionic stray current formation between galvanically isolated, parallel cells with common electrolyte supply was investigated. For this purpose, an ionic 4-point measurement setup was developed to experimentally determine the potential difference ΔE between parallel electrochemical cells. This systematic and transferable experimental approach was validated on an experimental setup with two parallel flow cells exemplary for alkaline water electrolysis. The measurement method is applicable to other systems and works with alternative technically relevant electrolytes. It was shown that stray currents in a parallel multi-cell system are determined by the potential difference ΔE between the cells and, therefore, depend on the individual cell voltages. Measurements were performed at 25, 40 and 60 °C. In the system presented, the relative dependence between the total stray current I_{sc} and the potential difference ΔE is 9.8, 12.3 and 16.5 mA/V at 25, 40 and 60 °C respectively. However, this correlation is explicitly valid only for the system tested in this study and depends on the electrolyte conductivity and the geometry of the tube manifold. Furthermore, the potential difference ΔE is also temperature dependent. However, the two temperature dependencies, i.e. of ΔE and of the ionic resistance of the electrolyte within the tube manifold R_t, compensate each other. Therefore, it was found that temperature has no measurable effect on the stray current if all other parameters are kept constant. By application of the ionic 4-point measurement, small stray currents of less than 1 % with respect to the cell current could be measured precisely in this study. When designing industrial plants, the influence of scaling parameters on stray currents must be taken into account [6,8]. During upscaling, the pipe cross-section of the electrolyte supply system is typically increased to manage the large volumes of electrolyte required. Increasing the cross-section without lengthening the pipe will increase the stray current in the system. This example shows that all scaling factors must be considered when designing a system to avoid exceeding critical stray current thresholds. It is therefore important to determine the total stray current a priori when designing new systems or industrial plants.

CRediT authorship contribution statement

Deniz Dogan: Writing – review & editing, Writing – original draft, Visualization, Validation, Methodology, Investigation, Formal analysis, Data curation, Conceptualization. **Burkhard Hecker:** Writing – review & editing, Supervision, Methodology, Conceptualization. **Bernhard Schmid:** Writing – review & editing, Methodology. **Hans Kungl:** Writing – review & editing, Funding acquisition. **Hermann Tempel:** Writing – review & editing, Supervision, Project administration, Funding acquisition, Conceptualization. **Rüdiger-A. Eichel:** Writing – review & editing, Supervision, Project administration, Funding acquisition, Conceptualization.

Declaration of competing interest

The authors declare that they have no known competing financial interests or personal relationships that could have appeared to influence the work reported in this paper.

Data availability

Data will be made available on request.

Acknowledgments

This work received funding by the German Federal Ministry of Education and Research (Bundesministerium für Bildung und Forschung, BMBF) under grant no. 03SF0627A "iNEW2.0 - Inkubator Nachhaltige Elektrochemische Wertschöpfungsketten".

Supplementary materials

Supplementary material associated with this article can be found, in the online version, at doi:10.1016/j.electacta.2024.144767.

References

[1] A.T. Kuhn, J.S. Booth, Electrical leakage currents in bipolar cell stacks, J. Appl. Electrochem. 10 (1980) 233–237, https://doi.org/10.1007/BF00726091.
[2] R. Qi, M. Becker, J. Brauns, T. Turek, J. Lin, Y. Song, Channel design optimization of alkaline electrolysis stacks considering the trade-off between current efficiency and pressure drop, J. Power Sources 579 (2023).
[3] X. Li, I. Sabir, Review of bipolar plates in PEM fuel cells: flow-field designs, Int. J. Hydrog. Energy 30 (2005) 359–371, https://doi.org/10.1016/j.ijhydene.2004.09.019.
[4] P.R. Prokopius, Model for calculating electrolytic shunt path losses in large electrochemical energy conversion systems, (1976) 12. https://ntrs.nasa.gov/search.jsp?R=19760014614.
[5] N.M. Delgado, R. Monteiro, J. Cruz, A. Bentien, A. Mendes, Shunt currents in vanadium redox flow batteries – a parametric and optimization study, Electrochim. Acta 403 (2022) 139667, https://doi.org/10.1016/j.electacta.2021.139667.
[6] G. Sakas, A. Ibáñez-Rioja, S. Pöyhönen, A. Kosonen, V. Ruuskanen, P. Kauranen, J. Ahola, Influence of shunt currents in industrial-scale alkaline water electrolyzer plants, Renew. Energy 225 (2024), https://doi.org/10.1016/j.renene.2024.120266.
[7] G. Hysa, V. Ruuskanen, A. Kosonen, M. Niemelä, L. Aarniovuori, D. Guilbert, J. Ahola, Effect of voltage elevation on cost and energy efficiency of power electronics in water electrolyzers, J. Power Sources 574 (2023), https://doi.org/10.1016/j.jpowsour.2023.233108.
[8] M. Rizwan, V. Alstad, J. Jäschke, Design considerations for industrial water electrolyzer plants, Int. J. Hydrog. Energy 46 (2021) 37120–37136, https://doi.org/10.1016/j.ijhydene.2021.09.018.
[9] E.A. Kaminski, R.F. Savinell, A technique for calculating shunt leakage and cell currents in bipolar stacks having divided or undivided cells, J. Electrochem. Soc. 130 (1983) 1103–1107, https://doi.org/10.1149/1.2119891.
[10] C. Yin, S. Guo, H. Fang, J. Liu, Y. Li, H. Tang, Numerical and experimental studies of stack shunt current for vanadium redox flow battery, Appl. Energy 151 (2015) 237–248, https://doi.org/10.1016/j.apenergy.2015.04.080.
[11] A.N. Colli, J.M. Bisang, A multi-region and open-source computational fluid dynamic tool for electrochemical systems with three-dimensional electrodes, AIChE J. 67 (2021) 1–15, https://doi.org/10.1002/aic.17371.
[12] N. Esfandiari, M. Aliofkhazraei, A.N. Colli, F.C. Walsh, S. Cherevko, L.A. Kibler, M. M. Elnagar, P.D. Lund, D. Zhang, S. Omanovic, J. Lee, Metal-based cathodes for hydrogen production by alkaline water electrolysis: review of materials, degradation mechanism, and durability tests, Prog. Mater. Sci. (2024) 101254, https://doi.org/10.1016/j.pmatsci.2024.101254.
[13] L.F. Arenas, C.P. De León, F.C. Walsh, C. Ponce de León, F.C. Walsh, Engineering aspects of the design, construction and performance of modular redox flow batteries for energy storage, J. Energy Storage 11 (2017) 119–153, https://doi.org/10.1016/j.est.2017.02.007.
[14] D. Pletcher, F.C. Walsh, Industrial Electrochemistry, Springer Science & Business Media, 2012.
[15] A.N. Colli, H.H. Girault, Compact and general strategy for solving current and potential distribution in electrochemical cells composed of massive monopolar and bipolar electrodes, J. Electrochem. Soc. 164 (2017) E3465–E3472, https://doi.org/10.1149/2.0471711jes.

[16] V.M. Schmidt, Elektrochemische Verfahrenstechnik. Grundlagen, reaktionstechnik, prozessoptimierung, 2004. 10.1002/ange.200385119.
[17] Y.S. Tsou, Current leakage through cascaded cells, Trans. Electrochem. Soc. 82 (1942) 353, https://doi.org/10.1149/1.3071420.
[18] J.C. Burnett, D.E. Danly, Current bypass in electrochemical cell assemblies, AIChE Symp. Ser. 75 (1979) 8–13.
[19] G. Codina, A. Aldaz, Scale-up studies of an Fe/Cr redox flow battery based on shunt current analysis, J. Appl. Electrochem. 22 (1992) 668–674, https://doi.org/10.1007/BF01092617.
[20] G. Codina, J.R. Perez, M. Lopez-Atalaya, J.L. Vasquez, A. Aldaz, Development of a 0.1 kW power accumulation pilot plant based on an Fe/Cr redox flow battery Part I. Considerations on flow-distribution design, J. Power Sources 48 (1994) 293–302, https://doi.org/10.1016/0378-7753(94)80026-X.
[21] M. Katz, Analysis of electrolyte shunt currents in fuel cell power plants, J. Electrochem. Soc. 125 (1978) 515–520, https://doi.org/10.1149/1.2131488.
[22] G.F. McLean, T. Niet, S. Prince-Richard, N. Djilali, An assessment of alkaline fuel cell technology, Int. J. Hydrog. Energy 27 (2002) 507–526, https://doi.org/10.1016/S0360-3199(01)00181-1.
[23] J.A. Schaeffer, L. Der Chen, J.P. Seaba, Shunt current calculation of fuel cell stack using Simulink®, J. Power Sources 182 (2008) 599–602, https://doi.org/10.1016/j.jpowsour.2008.04.014.
[24] G. Zhou, L. Der Chen, J.P. Seaba, CFD prediction of shunt currents present in alkaline fuel cells, J. Power Sources 196 (2011) 8180–8187, https://doi.org/10.1016/j.jpowsour.2011.04.029.
[25] F.T. Wandschneider, S. Röhm, P. Fischer, K. Pinkwart, J. Tübke, H. Nirschl, A multi-stack simulation of shunt currents in vanadium redox flow batteries, J. Power Sources 261 (2014) 64–74, https://doi.org/10.1016/j.jpowsour.2014.03.054.
[26] Q. Ye, J. Hu, P. Cheng, Z. Ma, Design trade-offs among shunt current, pumping loss and compactness in the piping system of a multi-stack vanadium flow battery, J. Power Sources 296 (2015) 352–364, https://doi.org/10.1016/j.jpowsour.2015.06.138.
[27] P.P. Pirotskii, N.N. Shvetsov, Instrument for measuring direct current in electrolyte jets, Meas. Tech. 12 (1961) 43–45.
[28] I. Roušar, V. Cezner, Experimental determination and calculation of parasitic currents in bipolar electrolyzers with application to chlorate electrolyzer, J. Electrochem. Soc. 121 (1974) 648, https://doi.org/10.1149/1.2401878.
[29] H. Fink, M. Remy, Shunt currents in vanadium flow batteries: measurement, modelling and implications for efficiency, J. Power Sources 284 (2015) 547–553, https://doi.org/10.1016/j.jpowsour.2015.03.057.
[30] E.R. Henquín, J.M. Bisang, Effect of leakage currents on the primary current distribution in bipolar electrochemical reactors, J. Appl. Electrochem. 37 (2007) 877–886, https://doi.org/10.1007/s10800-007-9324-2.
[31] E.R. Henquín, J.M. Bisang, Effect of leakage currents on the secondary current distribution in bipolar electrochemical reactors, J. Appl. Electrochem. 38 (2008) 1259–1267, https://doi.org/10.1007/s10800-008-9550-2.
[32] C. Comninellis, E. Plattner, P. Bolomey, Estimation of current bypass in a bipolar electrode stack from current-potential curves, J. Appl. Electrochem. 21 (1991) 415–418, https://doi.org/10.1007/BF01024577.
[33] B. Endrődi, G. Bencsik, F. Darvas, R. Jones, K. Rajeshwar, C. Janáky, Continuous-flow electroreduction of carbon dioxide, Prog. Energy Combust. Sci. 62 (2017) 133–154, https://doi.org/10.1016/j.pecs.2017.05.005.
[34] V. Liso, G. Savoia, S.S. Araya, G. Cinti, S.K. Kær, Modelling and experimental analysis of a polymer electrolyte membrane water electrolysis cell at different operating temperatures, Energies 11 (2018), https://doi.org/10.3390/en11123273.
[35] M. Ni, M.K.H. Leung, D.Y.C. Leung, Parametric study of solid oxide steam electrolyzer for hydrogen production, Int. J. Hydrog. Energy 32 (2007) 2305–2313, https://doi.org/10.1016/j.ijhydene.2007.03.001.
[36] P. Trinke, P. Haug, J. Brauns, B. Bensmann, R. Hanke-Rauschenbach, T. Turek, Hydrogen crossover in PEM and alkaline water electrolysis: mechanisms, direct comparison and mitigation strategies, J. Electrochem. Soc. 165 (2018) F502–F513, https://doi.org/10.1149/2.0541807jes.
[37] A.L. Santos, M.J. Cebola, J. Antunes, D.M.F. Santos, Insights on the performance of nickel foam and stainless steel foam electrodes for alkaline water electrolysis, Sustain (2023) 15, https://doi.org/10.3390/su151411011.
[38] A.N. Colli, H.H. Girault, A. Battistel, Non-precious electrodes for practical alkaline water electrolysis, Materials 12 (2019) 1–17, https://doi.org/10.3390/ma12081336 (Basel).
[39] G. Zhang, H. Wang, J. Yang, Q. Zhao, L. Yang, H. Tang, C. Liu, H. Chen, Y. Lin, F. Pan, Temperature effect on co-based catalysts in oxygen evolution reaction, Inorg. Chem. 57 (2018) 2766–2772, https://doi.org/10.1021/acs.inorgchem.7b03168.
[40] R.J. Gilliam, J.W. Graydon, D.W. Kirk, S.J. Thorpe, A review of specific conductivities of potassium hydroxide solutions for various concentrations and temperatures, Int. J. Hydrog. Energy 32 (2007) 359–364, https://doi.org/10.1016/j.ijhydene.2006.10.062.